

Dual Cross-Linked Functional Layers for Stable and Efficient Inverted Perovskite Solar Cells

Jing Zhou, Haixin Wang, Jianan Wang, Rui Chen, Sanwan Liu, You Gao, Yongyan Pan, Fumeng Ren, Xin Meng, Zhichun Yang,* Zonghao Liu,* and Wei Chen*

The operational stability of p–i–n perovskite solar cells (PSCs) is dramatically subjected to the quality of the perovskite light harvester and the interface layer atop the perovskite. Herein, a dual crosslinked functional layer strategy of using the versatile polydimethylsiloxane as an additive both in the perovskite layer and in phenyl-C61-butyric acid methyl ester interface layer, to improve the device tolerance against light, thermal, humidity, and bending stress, is reported. As a result, a promising power conversion efficiency of 21.6% (stabilized at 21.3%) for nickel oxide-based p–i–n PSCs is achieved. In addition, the unencapsulated devices maintain 97% of their initial efficiencies after continuous operation under 1 sun equivalent illumination at 60 °C with maximum power point tracking for 1000 h and 80% of their initial efficiencies exposed in ambient air for 500 h. The application of the aforementioned strategy in the flexible device also improves the bending mechanical stability, of which the corresponding flexible devices maintain 85% of their initial efficiencies after 1000 cycles at a radius of 8 mm.

1. Introduction


The record power conversion efficiency (PCE) of single-junction perovskite solar cells (PSCs) has skyrocketed to 25.7% after rapid development in the last decade.^[1] The p–i–n PSCs has

J. Zhou, H. Wang, J. Wang, R. Chen, S. Liu, Y. Gao, Y. Pan, F. Ren, X. Meng, Z. Liu, W. Chen
Wuhan National Laboratory for Optoelectronics (WNLO)
Huazhong University of Science and Technology (HUST)
Wuhan 430074, China
E-mail: liuzonghao@hust.edu.cn; wnlochenwei@hust.edu.cn

Z. Yang
State Key Lab of Quantum Optics and Quantum Optics Devices
Institute of Laser Spectroscopy
Shanxi University
Taiyuan 030006, China
E-mail: yangzhichun@sxu.edu.cn

Z. Yang
Collaborative Innovation Center of Extreme Optics
Shanxi University
Taiyuan 030006, China

Z. Liu, W. Chen
Optics Valley Laboratory
Wuhan 430074, China

 The ORCID identification number(s) for the author(s) of this article can be found under <https://doi.org/10.1002/solr.202300230>.

DOI: 10.1002/solr.202300230

demonstrated remarkable performance with negligible hysteresis,^[2] reliable operation, and good compatibility with state-of-the-art tandem devices.^[3] However, it is still inevitable to encounter the instability of the perovskite layer and the commonly used electron-transport layer (ETL) of phenyl-C61-butyric acid methyl ester (PCBM),^[4] delaying further improvement on the device stability.^[1b,5] With regard to the perovskite layer issue, the main reason is that perovskite material is vulnerable to humidity, thermal, ultraviolet light, and ion migration.^[6] In addition, a higher defect density will also accelerate the decomposition process of perovskite under light or thermal.^[7] As for the PCBM layer, it is sensitive to humidity and will auto-aggregate under continuous light and/or thermal due to its relatively weak intermolecular interaction.^[8] In addition, it allows I[−] to

diffuse from the perovskite layer to the metal electrode, which is unfavorable to the long-term stability of the device.^[9] Thus, strategies for both enhancing the intrinsic stability of perovskite including decreasing the defect density and improving its ability against humidity, light, and thermal stress as well as enhancing the intermolecular interaction of PCBM are very necessary to further prolong the operational stability of p–i–n PSCs.

Additive engineering of perovskite precursor has been widely investigated to regulate crystal growth or defect passivation for efficient and stable PSCs,^[10] including Lewis acid,^[11] Lewis base,^[12] alkyl ammonium salt,^[13] low-dimensional perovskite,^[14] or ionic liquid,^[15] and so on. Along with the evolution of these additive strategies,^[10a,b] a kind of additive with cross-linking effect stands out,^[16] which can suppress ions migration and meanwhile passivate defects at grain boundaries.^[16a,17] Recently, Song et al. introduced poly(ethylene glycol) dimethacrylate (PEGDMA) into perovskite precursor ink, achieving an effective chemically anchor at the grain boundaries, regulating the crystallization and reducing grain-boundary defects by the in situ cross-linking polymerization after thermal annealing process of perovskite films. In addition, the in situ cross-linking of PEGDMA can limit the thermal expansion of perovskites during thermal annealing, which released the residual strain to enhance the mechanical stability of the perovskite film.^[18] Sun et al. adopt a cross-linking oligomer of trimethylolpropane ethoxylate triacrylate to improve both the efficiency and stability of PSCs.^[19] However, polymer additives usually lead to precipitate in the

prepared perovskite precursor solution due to its strong interaction with PbI_2 and decreasing the grain size of perovskite film although polymers are more effective for both efficiency and stability improvement compared with small-molecule additives that is mainly working in efficiency improvement.^[20]

To enhance the stability of PCBM, quantum dots such as carbon, CdSe, or others,^[9a,21] polymers such as polystyrene; poly(methyl methacrylate); or others,^[4a,22] organic small molecule such as piperazine,^[23] and surfactants such as Triton X-100 and oleamide,^[24] graphene,^[25] and some other compounds have been used as dopants. These additives usually result in the enhanced charge-transfer capacity, hydrophobicity, and light stability of PCBM, which are beneficial for a high-efficiency and stable PSCs.^[26] For example, Cao et al. used PCBM doped with carbon quantum dots, realizing a 13% PCE enhancement of and the doped PCBM can prevent I^- migrating from perovskite layer for stable PSCs.^[9a] Jang et al. modified PCBM with Triton X-100, reducing interface carrier recombination and enhancing the air stability of PSCs.^[24a] Actually, these strategies are mainly working in solving the poor conductivity and uneven coverage of PCBM layer, and their improvements to the intrinsic stability of PCBM are generally limited.^[4a,9a,21b,24a,25a,27] Despite such methods involved in the stability enhancement of PSCs,^[28] the research for improving both perovskite and PCBM stability to enhance the performance of p–i–n PSCs is particularly desired.^[29]

In this work, we proposed a feasible dual cross-linked functional layers strategy by using polydimethylsiloxane (PDMS) cross-linking agent to synchronously cross-link the perovskite light harvester and PCBM layer. PDMS was introduced into the used antisolvent of chlorobenzene (CB) with an appropriate weight percentage to form PDMS:CB for the fabrication of high-quality perovskite film instead of adding into the perovskite precursor solution directly in case of the undesired precipitate and it was incorporated into the PCBM solution to construct a crosslinking ETL, respectively. On the one hand, thermal admittance spectroscopy (TAS) is used to investigate the sufficiently suppressed ion migration and the enhanced device stability against light, thermal, moisture, and bending was also demonstrated. The unencapsulated devices exhibit a long-term stability under 60 °C and 1 sun equivalent illumination (97% of initial efficiency after 1000 h), 80% of their original efficiency exposed in ambient air for 500 h, and 85% of their initial efficiency after bending 1000 times with a bending radius of 8 mm. On the other hand, the dual cross-linking functional layers strategy is demonstrated an effective strategy for suppressing the carrier non-radiative combination by time-resolved photoluminescence (TRPL), photoluminescence quantum yield (PLQY), light intensity-dependent on open-circuit voltages (V_{OC}), and transient photo-voltage (TPV). A hydron interaction between formamminium (FA) cation and PDMS as well as a Lewis acid–base coordination between the uncoordinated lead ions (Pb^{2+}) in perovskite and O donor of PDMS are verified by X-ray photoelectron spectroscopy (XPS), Fourier-transform infrared (FTIR) spectroscopy, and nuclear magnetic resonance (NMR). Decreased work functions (WF) of both perovskite and PCBM for a much more matched energy alignment and the passivation of grain boundaries in perovskite film are confirmed by ultraviolet photoelectron spectroscopy (UPS) and Kelvin probe force microscopy (KPFM) measurements. In addition, the device fabricated

with the dual cross-linked functional layers strategy exhibits an impressive efficiency of 21.6% (stabilized at 21.3%), the short-circuit current density (J_{SC}) and fill factor (FF) also up to 24.1 mA cm^{-2} and 82.8%, respectively, which is a top-level device performance of p–i–n PSCs with the inorganic nickel oxide-based hole-transport layer. This strategy is prospective to further promote the development of highly stable and efficient flexible devices.

2. Results and Discussion

The dual cross-linked functional layers strategy proposed in this work is using PDMS:CB as antisolvent for the preparation of high-quality perovskite film and PDMS is used as an additive for PCBM (**Figure 1**). As shown in Figure S1, Supporting Information, PDMS will occur cross-linking after thermal annealing in the presence of a curing agent, which is consistent with the previous report.^[30] For simplicity, the cross-linked perovskite absorber (CA) refers to the perovskite film prepared with PDMS:CB antisolvent, while the cross-linked PCBM ETL (CE) refers to the PCBM film with PDMS additive. The reference (Ref) film or device was prepared in terms of our previous report.^[31] With regard to CA, the optimal PDMS weight percentage is 0.045 wt% to CB (Figure S2, Supporting Information). The antisolvent was dropped after 15 s when the spin-coating procedure was activated, and then the sample was annealed at 150 °C for 30 min (Figure 1a). For the CE sample, PDMS and PCBM were dissolved in CB, in which the optimal PDMS weight percentage is 0.08 wt% to CB (Figure S3, Supporting Information). Then, the mixed PCBM solution (20 mg mL^{-1} , in CB) was spin-coated on top of the perovskite film as ETL and annealed at 70 °C for 10 min (Figure 1b). Finally, both cross-linking strategies were integrated, referred to CA&CE (Figure 1c and S4, Supporting Information).

To investigate the impact of individual crosslinking strategy (CA or CE) as well as dual cross-linking strategy (CA&CE) on the performance of p–i–n PSCs, devices with a standard structure of F-doped tin oxide (FTO)/NiMgLiO/perovskite/PCBM/bathocuproine (BCP)/Ag were prepared (**Figure 2a**). Figure 2b and Table S1, Supporting Information, show the current density–voltage (J – V) curves and photovoltaic (PV) parameters of the champion devices. The corresponding PV parameters including V_{OC} , J_{SC} , FF, and PCE are shown in Figure 2c. The champion Ref device exhibits a PCE of 19.36% with a V_{OC} of 1.062 V, J_{SC} of 22.96 mA cm^{-2} , and FF of 79.4%. The champion CA device exhibits an increased J_{SC} and FF, which is attributed to the reduced defects in perovskite film. The best-performing CE device shows a slightly improved V_{OC} and a significant improved J_{SC} , which is attributed to the reduced interface charge recombination and the improved PCBM coverage. Further detailed analyses are provided in the following section. Upon dual cross-linking, all PV parameters are enhanced compared with the Ref one, which demonstrates an improved PCE of 21.6% for the champion CA&CE device (Figure 2d). Furtherly, a stabilized PCE (under maximum power point [MPP] tracking for 300 s) of 21.3%, V_{OC} of 1.085 V, and J_{SC} of 23.8 mA cm^{-2} were achieved (Figure 2e). It is a top-level device performance of p–i–n PSCs with nickel oxide-based

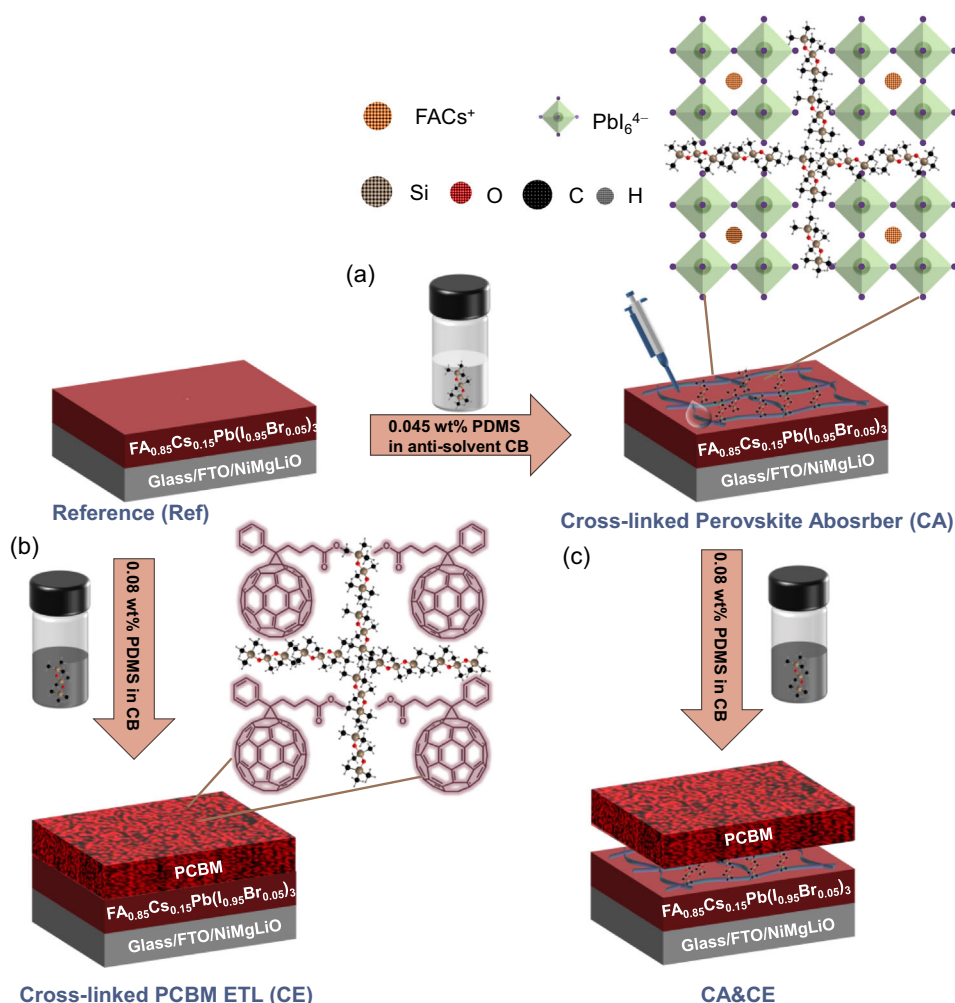


Figure 1. Schematic of perovskite absorber and phenyl-C61-butyrac acid methyl ester (PCBM) electron-transport layer (ETL) deposition process involving dual cross-linking strategy proposed in this work: a) cross-linked perovskite absorber (CA) by employing polydimethylsiloxane:chlorobenzene (PDMS:CB) as antisolvent for the spin-coating of perovskite film, b) cross-linked PCBM ETL (CE) by using PDMS as additive into the solution, and c) combination of CA and CE (CA&CE).

hole-transport layer as exhibited in Figure S5 and Table S2, Supporting Information. The external quantum efficiency (EQE) results of the best devices are shown in Figure S6, Supporting Information, the devices with dual cross-linked functional layers exhibits higher EQE in the whole visible spectrum. All these results indicate that the proposed strategy is beneficial for the performance of PSCs.

The relationship between V_{OC} and light intensity was further performed (Figure 3a), and the Ref, CA, CE, and CA&CE device exhibit slopes of 1.79, 1.47, 1.52, and 1.31 $k_B T/q$, respectively. k_B is the Boltzmann constant, T is the temperature and q is the electric charge. It is well known that deviation of the slope from $k_B T/q$ reflects defect-assisted recombination in PSCs, the lower slope indicates less carrier recombination.^[32] These results revealed that the devices with both CA and CE are helpful to suppress the carrier recombination. In addition, we conducted TPV and transient photo-current (TPC) measurements to investigate the charge recombination (τ_r) and transport (τ_t) under open- and short-circuit conditions, respectively. As shown in Figure 3b, τ_r

of the Ref, CA, CE, and CA&CE devices are 0.32, 0.61, 0.46, and 0.97 ms, respectively. The longer τ_r are attributed to the suppressed charge recombination. As shown in Figure S7, Supporting Information, the τ_t values are 7.45, 4.30, 5.80, and 3.75 μ s, respectively. The decreased τ_t is ascribed to a reduced charge recombination or an increased electron extraction ability. Further, PLQY was employed to quantify the reduction of non-radiative recombination, which is associated with internal quasi-Fermi level splitting (QFLS) determining the V_{OC} level.^[33] The stacked FTO/NiMgLiO/perovskite without ETL was first analyzed, exhibited in Figure S8, Supporting Information, the PLQY values of Ref and CA sample are 7.5% and 7.9%, respectively. According to the equation reported previously as follows^[34]

$$\Delta QFLS = 25.7 \text{ meV} \times \ln \left(\frac{PLQY_{\text{passivated}}}{PLQY_{\text{ref}}} \right) \quad (1)$$

The calculated QFLS difference is just 1.31 meV, which is reflecting a negligible V_{OC} increase between the Ref and CA samples. It

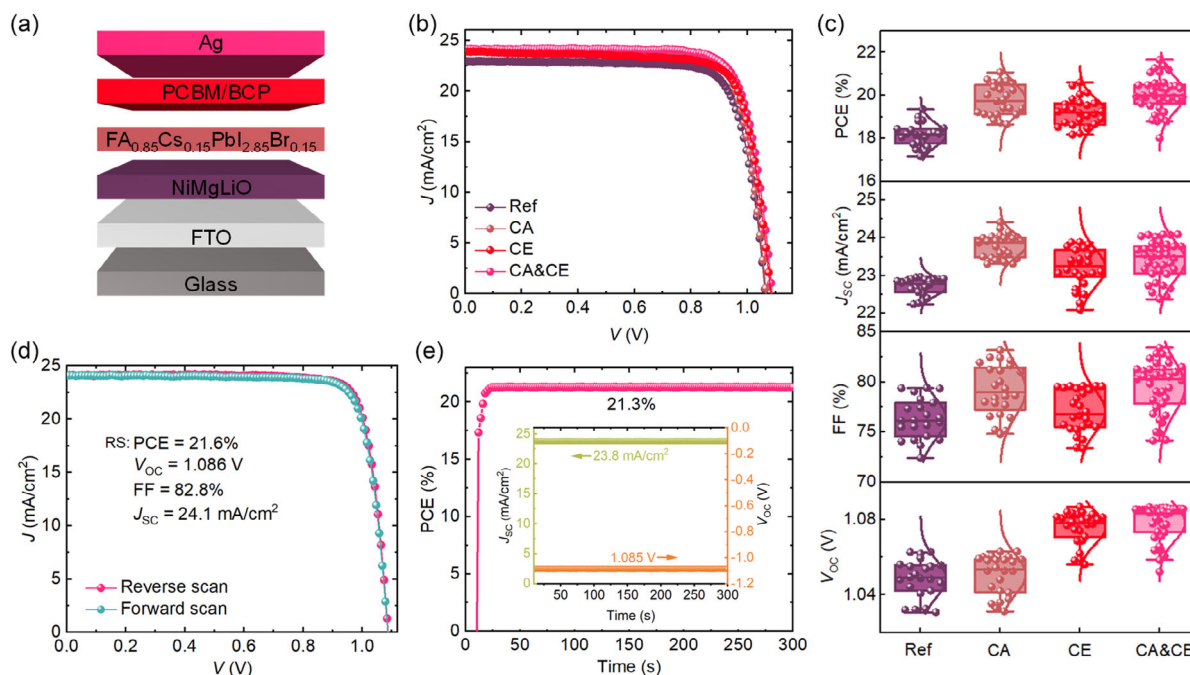


Figure 2. a) Schematic diagram of device structure FTO/NiMgLiO/perovskite/PCBM/BCP/Ag. b) Current density–voltage (J – V) curves and c) the statistical graphic of photovoltaic parameters about the PSCs without any modification, with single perovskite absorber cross-linked (CA), with single PCBM ETL cross-linked (CE) and combined perovskite absorber cross-linked with PCBM ETL cross-linked (CA&CE). d) J – V curve and e) the stabilized power conversion efficiency (PCE), short-circuit current density (J_{sc}), and open-circuit voltages (V_{oc}) under maximum power point (MPP) of the device with best performance.

indicates a high quality of our perovskite film, which does not limit the V_{oc} .^[35] Then, the whole device with ETL is characterized in Figure 3c, in which PLQY results for Ref, CA, CE, and CA&CE are 0.062%, 0.065%, 0.1%, and 0.11%, respectively. It is obviously that there is a significantly increased of QFLS after PCBM cross-linking was introduced, where the Δ QFLS between Ref and CE was 12.07 meV according to Equation (1). Moreover, the CA sample exhibits a slight impact on the QFLS, these results are consistent with the change of V_{oc} . It can be recognized by the following two aspects, one is the interface of perovskite/PCBM-weakened voltage of the device, and the other is the cross-linked PCBM that can inhibit the interface recombination to some extent.^[35] To further investigate the source of V_{oc} change, we analyze the built-in potentials (V_{bi}) of the Ref, CA, CE, and CA&CE devices by Mott–Schottky (M–S) measurement (Figure 3d). According to the equation

$$\frac{1}{C^2} = \frac{2(V_{bi} - V)}{q\epsilon\epsilon_0 A^2 N} \quad (2)$$

where q is the elementary charge quantity, V is the bias applied during the test, N is the impurity concentration, A is the active area of the device, and ϵ and ϵ_0 are relative dielectric constant of perovskite absorber and vacuum dielectric constant, respectively. V_{bi} can be obtained from the intersection of the line in the linear region of the M–S graph and the line of $\frac{1}{C^2} = 0$. The CE and CA&CE devices exhibit higher V_{bi} of 0.92 V than the Ref and CA devices of 0.88 V, which shows similar regularity with the PLQY measurement. The enhanced V_{bi} is relevant with the

reduction of defects and suppressed recombination at perovskite surface, which contributes to larger V_{oc} . It seems that the mechanism why CA sample demonstrated an improved device performance is still not clear, since the QFLS difference between the Ref and CA samples are indistinctive. To focus on this point, the lifetime of glass/perovskite stacks were characterized by TRPL (Figure S9, Supporting Information) and the CA film (502 ns) exhibits a longer lifetime than the Ref film (300 ns). With regard to this result, we propose the enhanced lifetime can be attributed to the decreased defects of perovskite interior,^[36] which are consistent with the enhancement of J_{sc} and FF for the CA device.^[37] To further validate it, we adopted space charge limited current (SCLC) measurements to evaluate the change of trap-state density (n_t) and charge-carrier mobility (μ) for the samples with different cross-linking strategies. As shown in Figure S10, Supporting Information, the electron-only devices with a structure of FTO/SnO₂/perovskite/PCBM/Ag were analyzed. According to the Mott–Gurney Equation (3) and (4)^[35a]

$$J = \frac{9}{8} \epsilon\epsilon_0 \mu \frac{V^2}{d^3} \quad (3)$$

$$V_{TFL} = \frac{qn_t d^2}{2\epsilon\epsilon_0} \quad (4)$$

From which the calculated electron mobility of the devices Ref, CA, CE, and CA&CE are 1.01×10^{-3} , 1.51×10^{-3} , 1.31×10^{-3} , and $2.01 \times 10^{-3} \text{ cm}^2 \text{ V}^{-1} \text{ s}^{-1}$, respectively. And, the calculated trap-state densities are 6.61×10^{15} , 3.63×10^{15} , 5.01×10^{15} ,

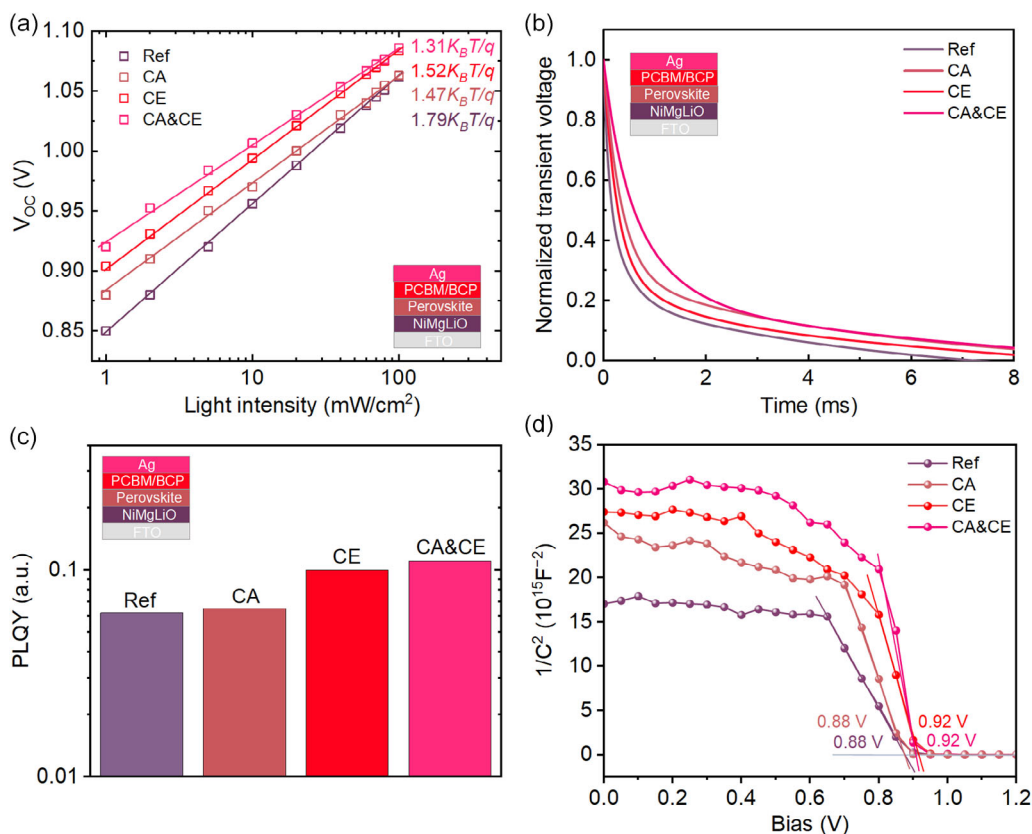


Figure 3. a) V_{OC} versus light intensity, b) normalized transient photovoltage decay curves, c) photoluminescence quantum yield (PLQY), and d) Mott-Schottky plots about the PSCs without any modification (Ref), with single-perovskite absorber cross-linked (CA), with single PCBM ETL cross-linked (CE) and combined perovskite absorber cross-linked with PCBM ETL cross-linked (CA&CE).

and $2.66 \times 10^{15} \text{cm}^{-3}$, respectively (Table S3, Supporting Information). Both the TRPL and SCLC results indicate that the individual CA or CE are all useful for enhancing the carrier mobility, and meanwhile decreasing the trap densities at interior and surface of the perovskite films.

Above all, we have demonstrated that the superior performance of our dual cross-linked functional layers strategy is feasible to reduce the non-radiative recombination at perovskite interior as well as the perovskite/PCBM interface. Then, how the cross-linking strategy affects the film morphology, crystallinity, energy band structure, and the corresponding passivation mechanism are also investigated. Scanning electron microscope (SEM) is carried out to characterize the film morphology (Figure S10, Supporting Information). As shown in Figure S11a,b, Supporting Information, the fabricated perovskite films with and without PDMS are uniform, while the CA film shows larger grain size. The average grain sizes of the Ref and CA films are 280 and 370 nm, respectively, which indicates that PDMS:CB antisolvent has a positive impact on the nucleation and crystal growth of perovskite films. This phenomenon can be related to the interaction between PDMS and perovskite precursors, which will be further studied in the next section.^[38] Figure S10c,d, Supporting Information, shows SEM images of PCBM with and without PDMS additive, and the film with PDMS cross-linker achieved a higher coverage and better

uniformity. This result can be ascribed to the increased solution viscosity and excellent film forming. A reduced roughness of the fabricated films are revealed by atomic force microscope (AFM), which is attributed to the formation of PDMS cross-linker at grain boundaries of perovskite film (Figure S12a,b, Supporting Information).^[35a] The cross-linked PCBM layer also exhibits a smaller roughness than the Ref one, and it can be verified from the $5 \times 5 \mu\text{m}$ images. Small pinholes are observed in the Ref PCBM layer, which is induced by the low viscosity of PCBM solution. And, it is more likely to form a compact film while the high-weight PDMS polymer is added into the PCBM solution (Figure S12c,d, Supporting Information).^[39] To study the effect of PDMS cross-linker to crystal structure of the prepared perovskite films, we conduct X-ray diffraction (XRD) measurements (Figure S13, Supporting Information). Diffraction peaks at about 14° , 20° , 28° , and 32° are corresponding to the (101), (012), (202), and (211) lattice plane of the $\text{FA}_{0.85}\text{Cs}_{0.15}\text{Pb}(\text{Br}_{0.15}\text{I}_{2.85})_3$ perovskite phase.^[40] It is obvious that the (101) and (012) lattice orientation are enhanced with PDMS:CB antisolvent, which indicates an improved crystal quality of perovskite film. This result is consistent with the increased grains.

XPS of the FTO/perovskite and FTO/PCBM samples are performed to investigate the passivation mechanism and confirm the existence of the cross-linker. The XPS spectra of Pb 4f, N 1s, O 1s, Si 2p, C 1s, Cs 3d, I 3d, and Br 3d are shown in

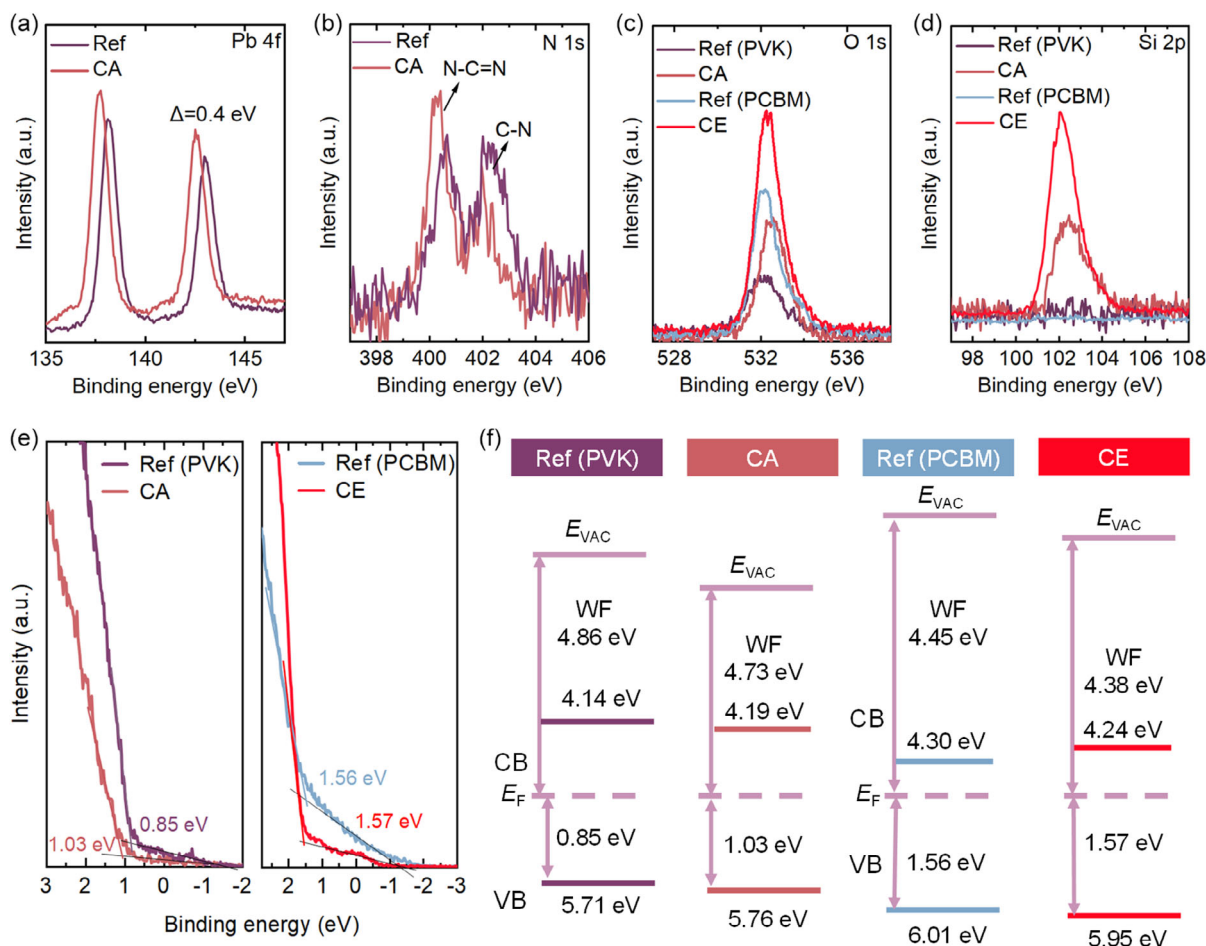


Figure 4. a–d) X-ray photoelectron spectroscopy (XPS) spectra, e, f) ultraviolet photoelectron spectroscopy (UPS) spectra of the perovskite films and PCBM films without any modification Ref perovskite (PVK), Ref (PCBM), CA, and cross-linked PCBM ETL (CE).

Figure 4a–d, S14, Supporting Information. It is obvious that the Pb 4f shifts toward lower binding energy after the perovskite film cross-linked by PDMS, indicating that a negative charge occurs around the Pb^{2+} . The uncoordinated Pb^{2+} can be coordinated with PDMS by accepting the lone-pair electrons on the oxygen atom in PDMS molecule, and the O 1s shifts toward higher binding energy due to the loss of electrons. It is noted that the O atom detected in the pristine perovskite film is attributed to the physisorption.^[41] In addition, N 1s also shifts toward lower binding energy, which is attributed to the hydrogen interaction between N and O atom.^[41b] In addition, Si is detected in CA and CE samples, and this result confirms the existence of PDMS in perovskite and PCBM films. To further confirm the interaction between PDMS and perovskite precursors, FTIR and NMR measurements are conducted for the samples with and without PDMS cross-linking. The pure PDMS is also characterized for comparison. As shown in Figure S15, Supporting Information, the peak around 800 and 1095 cm^{-1} is the symmetric stretching vibration peak and antisymmetric stretching vibration of Si–O–Si, respectively, which are all signed as #. Several aspects can be observed from the FTIR spectra. First, both the CA and CE samples present the Si–O–Si stretch, and it further confirms the existence of

PDMS in the films together with XPS result. Second, the Si–O–Si symmetric stretching vibration peak shifts toward higher wavenumber in the CA sample compared with pure PDMS, indicating the interaction between PDMS and perovskite films. Finally, the peak at 1712 cm^{-1} corresponds to C=N stretching vibration, after PDMS cross-linking, and the peak shifts to higher wavenumber can be ascribed to the hydrogen interaction between PDMS and the FA cation. To further confirm the existence of hydron interaction, the NMR measurement is carried out for formamidinium iodide (FAI), PDMS, and FAI + PDMS samples. As shown in Figure S16, Supporting Information, 8.96 ppm of the pure FAI is the resonance of an active proton on an amino group, and the hydrogen bond makes the chemical shift toward higher ppm.^[42]

UPS measurement is adopted to evaluate the effect of the cross-linker to the energy level of the fabricated films. According to the secondary electron cutoff spectra, valance band spectra from UPS and bandgap result obtained by ultraviolet–visible absorption (UV–vis) spectra (Figure 4e, S17, S18, Supporting Information), and we can deduce the energy band illustration (Figure 4f and Table S4, Supporting Information). The WF of Ref perovskite film and PCBM film is 4.86 and

4.45 eV, respectively. The valence band position of the Ref perovskite film and PCBM film is 5.71 and 6.01 eV, respectively. These results are consistent with the previous reports.^[31,43] For the CA sample, the WF decreased to 4.73 eV and the valence band is 5.76 eV, indicating an n-type perovskite is formed while the Fermi level shifts toward conduction band. Moreover, it is resulted from the decreased electron trap density, which is consistent with the SCLC results, including the reduced FA vacancies owing to the formation of hydrogen bond and the reduced uncoordinated Pb defects.^[35a,43] For the CE sample, the WF decreased from 4.45 to 4.38 eV, and the valence band position is 5.95 eV. The Fermi level of PCBM shifts toward LUMO energy level after PDMS cross-linking, indicating an n-doping of PCBM for better electron-transport ability (Figure S19, Supporting Information).^[44] In addition, a much more matched energy alignment facilitates the electron extraction and transport at the perovskite/PCBM interface (Figure S20, Supporting Information), which can also be verified by the TPC result.

In consequence, an effective dual cross-linked functional layers strategy has been verified to passivate the defects at the bulk and surface of perovskite film and improve the film formation of PCBM layer, which facilitates an appropriate the energy-level structure enabling an efficient electron extraction and transport. Subsequently, KPFM measurement is performed to investigate the PDMS cross-linker at the perovskite layer mainly working by the defects passivation at the grain bulk or boundaries, which can reflect the potential distribution of the sample surface by the contact potential difference (CPD) between the metal needle and the sample surface.^[35a,45] The samples of FTO/NiMgLiO/perovskite, FTO/NiMgLiO/CA, FTO/NiMgLiO/perovskite/PCBM, and FTO/NiMgLiO/perovskite/CE are studied. It can be found that the CA and CE samples exhibit higher CPD than the counterpart of the Ref, which can be explained by the decreased WF discussed earlier. To figure out the CPD changes at grain boundaries with respect to the internal crystals of CA and Ref samples, the CPD difference between the grain and grain boundaries are analyzed (Figure S21, Supporting Information). For comparison, we set CPD inside the crystal to zero. The CPD of the Ref and CA sample are about 0–200 and 0–150 mV, respectively. The higher CPD at the grain boundary than the grain bulk corresponds to the accumulated electron at the grain boundaries^[46] and the reduction of the CPD attributes to the passivated grain boundaries.^[35a] The CPD distribution of the perovskite film samples over large area demonstrates that the Ref perovskite film fluctuated distinctly as shown in Figure S22, Supporting Information, indicating much more defects at the grain boundaries. However, it exhibits a flat CPD change trend for CA sample, from which less defects at grain boundaries are proposed furtherly. As for the cross-linked PCBM, it is obvious that the CE sample is relatively smoother than the Ref PCBM, owing to the preferable film uniformity.

To evaluate the light and thermal stability of the cross-linked perovskite and PCBM layer, the film morphology and electrical conductivity were checked by C-AFM after aging at 120 °C under 1 sun equivalent white light emitting diode (LED) illumination in N₂ atmosphere for 50 h (Figure S23, Supporting Information). Obviously, a significantly enhanced light–thermal stability is demonstrated for the perovskite and PCBM film after cross-linking process. For the Ref perovskite film, its initial morphology is

clear and the current can be detected accompanied with the grain profile (Figure S23a,b, Supporting Information) while the morphology is blurry after aging and the current mapping shows no grain structure but just instrument noise (Figure S23e,f, Supporting Information), which indicates that the perovskite film was degraded seriously after subjecting to the stress of light and heat. With regard to the cross-linked perovskite layer, the morphology and current mapping are intact after aging, indicating a good light–thermal stability (Figure S23i,j,m,n, Supporting Information). The positive effect of cross-linked perovskite against light–thermal stress can be attributed to the suppressed ion migration induced by the reduced defects at grain boundary and surface of the perovskite film, resulting an improved device stability discussed later. Furthermore, for the Ref PCBM film, its initial current is about 8 nA, while there is no current signal after aging process. The morphology exhibits a big lump from the initial graininess, and confirms PCBM can be auto-aggregated under light and/or thermal stress, inducing an inferior conductivity (Figure S23c,d,g,h, Supporting Information), which is consistent with previous report.^[47] In contrast to the Ref one, the cross-linked PCBM film remains the initial current distribution and morphology after aging (Figure S23k,l,o,p, Supporting Information), which indicates a much higher light–thermal stability after cross-linking. Considering that the defects will accelerate ion migration, and loose PCBM structure also allows ion migrate through it toward metal electrode inducing the degradation of the perovskite.^[36a] While we have demonstrated that our dual cross-linking strategy can reduce the defects at grain boundary and surface of the perovskite film, and cross-linked PCBM has a better compact structure with enhanced light–thermal stability, which seems that this strategy also can suppress ion migration of the perovskite device. Then, TAS was employed to obtain the ion-migration active energy of the Ref, CA, CE, and CA&CE samples. Figure S24a–d, Supporting Information, shows the TAS spectra of the devices tested from 278 to 318 K. The corresponding E_a is calibrated according to the equation

$$\omega_{\text{peak}} = \beta T^2 \exp(-E_a/k_B T) \quad (4)$$

where β is temperature-independent prefactor, T is the absolute temperature, k_B is the Boltzmann constant, and ω_{peak} is the angular frequency obtained by the maxima of the capacitance differential derivative (Figure S24e–h, Supporting Information). The calibrated E_a are 114, 155, 140, and 170 meV, respectively (Figure 5a, S25, Supporting Information). The increased E_a indicates the passivation of grain boundaries and perovskite surface can enhance the ion-migration barrier. The increased ion-migration barrier and enhanced light–thermal stability of the perovskite and PCBM layer pave an avenue for the long-term photothermal stability of the devices. Then, the long-term device thermal stability and light–heat stability were carried out as shown in Figure 5b,c.^[48] The heat stability was checked under a severe temperature of 85 °C (dark, in N₂ atmosphere). The light–heat stability was performed under 1 sun equivalent illumination at 60 °C in N₂ atmosphere and MPP tracking condition. The Ref devices only maintain 48% and 43% of their initial efficiency after 500 h thermal and 1000 h light–heat aging test, while the CA&CE samples can retain 89% and 97% of their initial

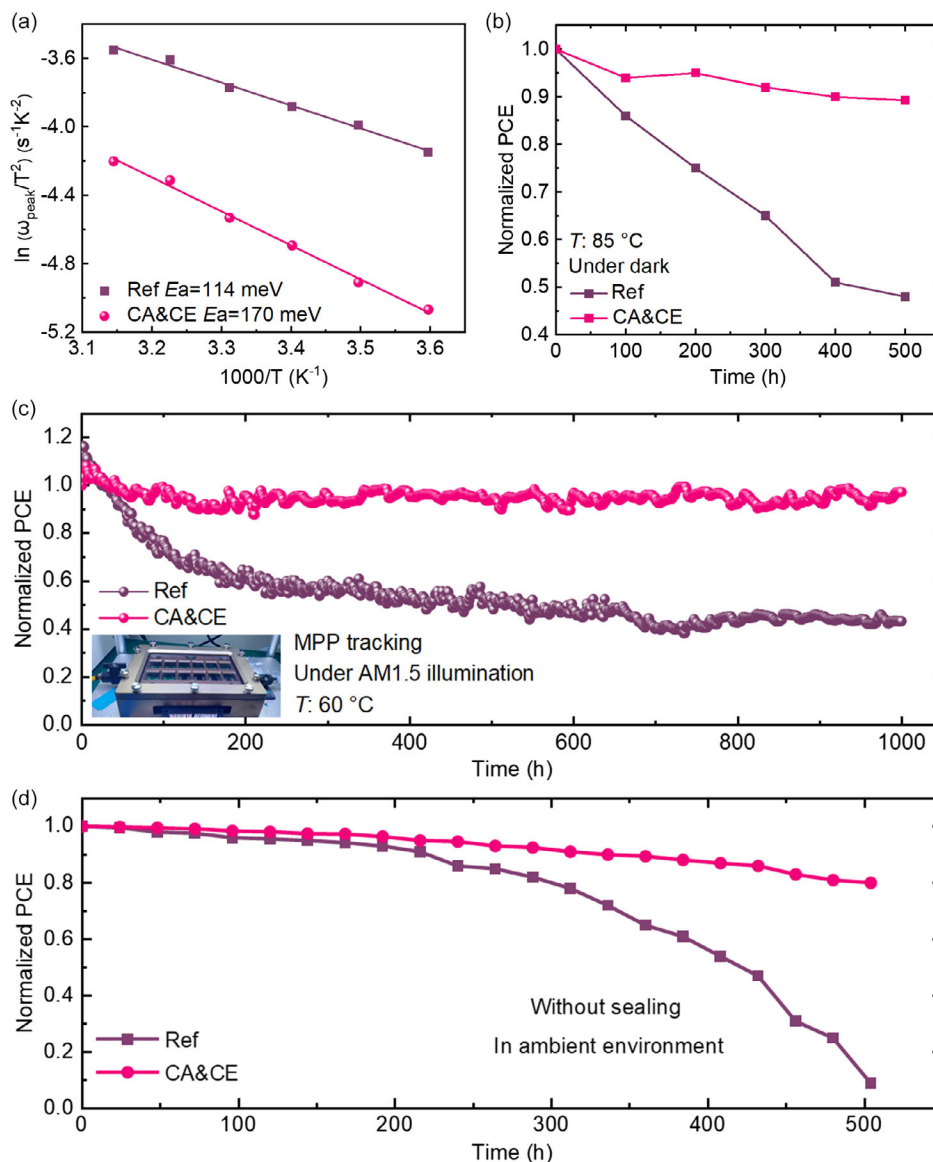


Figure 5. a) The E_a of the Ref and CA&CE samples obtained from the thermal admittance spectroscopy (TAS) spectra. b) Thermal stability test of the Ref and CA&CE samples under 85 °C in dark at N_2 atmosphere. c) Light–thermal stability test of the Ref and CA&CE samples under 1 sun equivalent illumination at 60 °C in N_2 atmosphere. d) The environment stability test of the Ref and CA&CE samples without encapsulation.

efficiency at the same condition. The laser beam–induced current (LBIC) measurement also further confirms the improved light-induced stability of the CA&CE sample (Figure S26, Supporting Information). It is noted that not only the CA but also the CE can improve the stability of the whole device. The moisture resistance of the samples is also evaluated. As is shown in Figure S27a, Supporting Information, the absorption spectrum and optical image of the CA&CE sample retain perfect, while the Ref one degrades seriously. In addition, the increased contact angle of the CA and CE samples also demonstrate an excellent moisture resistance capability of the cross-linked samples, which can be attributed to the doped PDMS and the formed hydrogen bond (Figure S27b–e, Supporting Information).^[49] And, the long-term moisture stability was also carried out as shown in Figure 5d, and the CA&CE sample also demonstrates an

improved environment stability. All the initial PV parameters of the devices with different aging conditions are shown in Table S5, Supporting Information.

Beyond that, owing to the low Young’s modulus of the organic PDMS polymer,^[50] the impact of the proposed dual cross-linked functional layers strategy on the flexibility of the films and devices are also tested. As shown in Figure S28a–d (Supporting Information), SEM is employed to check the microstructure of the perovskite and PCBM films after bending. Obvious cracks are observed on the Ref samples, while the CA and CE samples have no this phenomenon. Furthermore, we also carried out the bending test of flexible device (Figure S28e, Supporting Information). The mechanical stability of the CA&CE devices demonstrates significantly better flexibility than the standard devices. After bending 1000 times with a radius of 8 mm, optical

images of the corresponding devices are shown in Figure S29, Supporting Information. All these results indicate the PDMS cross-linker can release the stress of the materials, thereby increasing the mechanical stability of the flexible devices, which is beneficial for the operational stability of PSCs. In summary, the device stabilities based on dual cross-linked functional layers are evaluated in various aspects, and the importance of cross-linking strategy for stable and efficient PSCs is emphasized.

3. Conclusions

In conclusion, we develop a feasible strategy of dual cross-linked functional layers employing both a CA and a cross-linked PCBM layer with the cross-linker of PDMS for p–i–n PSCs, which can reduce the defects at the grain boundaries and surface of the perovskite film. Meanwhile, the PDMS additive can improve the viscosity of solution and increase the film-forming ability of PCBM. Finally, the dual cross-linked device achieves an improved PCE of 21.6% with significantly enhanced J_{SC} and FF. In addition, the stability of both the perovskite and PCBM layer are improved, resulting in an enhanced ion-migration activation energy of the whole device. All these facilitate the enhanced light, thermal, moisture, and mechanical stability of the devices.

4. Experimental Section

Materials: FAI ($\text{CH}(\text{NH}_2)_2\text{I}$ (FAI), 99.5%), lead (II) iodide (99.99% metals basis), cesium bromide (>99%), and bathocuproine (>99%) were purchased from Tokyo Chemical Industry Co., Ltd. All other chemicals were purchased from Sigma–Aldrich and used as received.

Device Fabrication: The studied Ref-, CA-, CE-, and CA&CE-based devices were prepared following the well-established procedure.^[31,51] FTO glasses (TEC-8, Nippon Sheet Glass Co., Japan) were etched and ultrasonically cleaned with the bath of detergent solution, distilled water, industrial alcohol, and alcohol for 20 min, respectively. Then, a p-type NiMgLiO film was deposited on top of the FTO glass: a mixture solution of acetonitrile and ethanol (with 95:5 volume ratio, 30 mL) of nickel acetylacetonate (with magnesium acetate tetrahydrate and lithium acetate, and the mole atomic ratios of Ni:Mg:Li is 80:15:5, the total metal-ion concentration is 0.02 mol L^{-1}) was sprayed by an air nozzle (with 0.2 mm caliber) onto the hot FTO glasses (570 °C). After spraying, the samples were further treated at 570 °C for another 40 min and then left to cool down naturally. After that, perovskite was deposited by the anti-solvent method. The $\text{FA}_{0.85}\text{Cs}_{0.15}\text{Pb}(\text{I}_{0.95}\text{Br}_{0.05})_3$ perovskite films were deposited by using a precursor solution containing FAI, PbI_2 , and CsBr in DMF:DMSO = 4:1 by volume. The PDMS as additive into the CB antisolvent was added as drops at 15th second of spin-coating. The PCBM solution was prepared by dissolving 20 mg PCBM in 1 mL of CB with PDMS as additive and was stirred vigorously at 45 °C overnight before spin-coating. PCBM was deposited on the FTO/NiMgLiO/perovskite substrate by spin-coating at 2000 rpm for 30 s at room temperature followed by a 70 °C thermal treatment for 10 min. Then BCP was spin-coated on PCBM at 6000 rpm for 30 s and annealed at 70 °C for 10 min. In the final step, Ag was deposited at a high vacuum (less than $5 \times 10^{-4} \text{ Pa}$) while finely controlling the evaporation rate at 0.1 and 0.1–0.5 Å s^{-1} , respectively.

Film Characterization: SEM images were carried out by using a Nova NanoSEM 450 SEM (FEI Co., Netherlands). The crystal structure of the films was characterized using XRD with an Empyrean X-ray diffractometer with Cu $K\alpha$ radiation (PANalytical B.V. Co., Netherlands). The TRPL studies were performed using an Edinburgh FLS920 fluorescence spectrometer (Edinburgh Co., UK). The UV–vis spectra were recorded using a

Lambda 950 spectrophotometer (PerkinElmer Co., USA). AFM and KPFM measurements were made by the SPM9700 produced from Shimadzu company of Japan. XPS and UPS were measured employing AXIS SUPPA + X-ray photoelectron spectrometer produced by Shimadzu Kratos of Japan.

Device Measurements: Light intensity-dependent V_{OC} , TPV, and TPC were measured by Zahner electrochemical workstation. PLQY of the devices were characterized by QuantaMaster 8000 steady-state transient modular fluorescence spectrometer made in HORIBA Canada. Admittance spectroscopy was obtained using a homemade combinatorial testing system mainly consisting of an impedance analyzer (Agilent E4980A LCR meter), a liquid nitrogen cryostat (Janis VPF-100), and a temperature controller (Lakeshore 325). PV measurements employed a black mask with an aperture area of 0.09 cm^2 under standard AM1.5G simulated sunlight (Oriol Class AAA, XES-160S1, SAN-EI ELECTRIC CO., LTD., Japan) with a source meter (Keithley 2601 B), and the simulated light intensity was calibrated with a silicon photodiode. The operational stability was measured with a multichannel-automated stability testing system (91PVKSolar Co., Ltd.), with maximum power point-tracking software, white LED arrays as the light source and an N_2 filled testing chamber as the holder of samples.

Supporting Information

Supporting Information is available from the Wiley Online Library or from the author.

Acknowledgements

J.Z. and H.W. contributed equally to this work. This work was supported by the National Key Research and Development Project funding from the Ministry of Science and Technology of China (Grant no. 2021YFB3800104), the National Natural Science Foundation of China (Grant nos. 52002140, U20A20252, and 62205187), Young Elite Scientists Sponsorship Program by CAST, the Self-determined and Innovative Research Funds of HUST (Grant no. 2020kfyXJJS008), the Natural Science Foundation of Hubei Province (Grant no. 2022CFA093), the Fundamental Research Program of Shanxi Province (Grant no. 202103021223032), the Innovation Project of Optics Valley Laboratory (Grant no. OVL2021BG008), and Fujian science & technology innovation laboratory for energy devices of China (21C LAB). The authors thank the Analytical and Testing Center of Huazhong University Science and Technology for the sample measurements.

Conflict of Interest

The authors declare no conflict of interest.

Data Availability Statement

The data that support the findings of this study are available from the corresponding author upon reasonable request.

Keywords

dual-crosslink, PCBM, perovskite solar cells, stability

Received: April 5, 2023

Revised: April 24, 2023

Published online:

- [1] a) Best Research-Cell Efficiency Chart, <https://www.nrel.gov/pv/cell-efficiency.html>, (accessed: December 2022); b) Q. Jiang, J. Tong, Y. Xian, R. A. Kerner, S. P. Dunfield, C. Xiao, R. A. Scheidt, D. Kuciauskas, X. Wang, M. P. Hautzinger, *Nature* **2022**, 611, 278.
- [2] X. Lin, D. Cui, X. Luo, C. Zhang, Q. Han, Y. Wang, L. Han, *Energy Environ. Sci.* **2020**, 13, 3823.
- [3] a) A. Al-Ashouri, E. Köhnen, B. Li, A. Magomedov, H. Hempel, P. Caprioglio, J. A. Márquez, A. B. Morales Vilches, E. Kasparavicius, J. A. Smith, *Science* **2020**, 370, 1300; b) A. Al-Ashouri, A. Magomedov, M. Roß, M. Jošt, M. Talaikis, G. Chistiakova, T. Bertram, J. A. Márquez, E. Köhnen, E. Kasparavičius, *Energy Environ. Sci.* **2019**, 12, 3356.
- [4] a) D. Yang, X. Zhang, K. Wang, C. Wu, R. Yang, Y. Hou, Y. Jiang, S. Liu, S. Priya, *Nano Lett.* **2019**, 19, 3313; b) D. Zhang, D. Li, Y. Hu, A. Mei, H. Han, *Commun. Mater.* **2022**, 3, 58; c) F. Zhang, W. Shi, J. Luo, N. Pellet, C. Yi, X. Li, X. Zhao, T. J. S. Dennis, X. Li, S. Wang, *Adv. Mater.* **2017**, 29, 1606806.
- [5] a) X. Li, S. Fu, W. Zhang, S. Ke, W. Song, J. Fang, *Sci. Adv.* **2020**, 6, eabd1580; b) C. H. Chiang, C. G. Wu, *ChemSusChem* **2016**, 9, 2666.
- [6] a) R. Wang, M. Mujahid, Y. Duan, Z.-K. Wang, J. Xue, Y. Yang, *Adv. Funct. Mater.* **2019**, 29, 1808843; b) J. Yang, B. D. Siempelkamp, D. Liu, T. L. Kelly, *ACS Nano* **2015**, 9, 1955.
- [7] a) Y. Shao, Y. Fang, T. Li, Q. Wang, Q. Dong, Y. Deng, Y. Yuan, H. Wei, M. Wang, A. Gruverman, *Energy Environ. Sci.* **2016**, 9, 1752; b) J. S. Yun, J. Seidel, J. Kim, A. M. Soufiani, S. Huang, J. Lau, N. J. Jeon, S. I. Seok, M. A. Green, A. Ho-Baillie, *Adv. Energy Mater.* **2016**, 6, 1600330; c) L. Liu, S. Huang, Y. Lu, P. Liu, Y. Zhao, C. Shi, S. Zhang, J. Wu, H. Zhong, M. Sui, *Adv. Mater.* **2018**, 30, 1800544.
- [8] a) J. Jia, J. Wu, J. Dong, L. Fan, M. Huang, J. Lin, Z. Lan, *Chem. Commun.* **2018**, 54, 3170; b) Y. Jiang, J. Wang, H. Zai, D. Ni, J. Wang, P. Xue, N. Li, B. Jia, H. Lu, Y. Zhang, *J. Am. Chem. Soc.* **2022**, 144, 5400.
- [9] a) X. Zhu, J. Sun, S. Yuan, N. Li, Z. Qiu, J. Jia, Y. Liu, J. Dong, P. Lv, B. Cao, *New J. Chem.* **2019**, 43, 7130; b) Z. Liu, J. Hu, H. Jiao, L. Li, G. Zheng, Y. Chen, Y. Huang, Q. Zhang, C. Shen, Q. Chen, *Adv. Mater.* **2017**, 29, 1606774.
- [10] a) F. Zhang, K. Zhu, *Adv. Energy Mater.* **2020**, 10, 1902579; b) A. Mahapatra, D. Prochowicz, M. M. Tavakoli, S. Trivedi, P. Kumar, P. Yadav, *J. Mater. Chem. A* **2020**, 8, 27; c) I. S. Yang, N. G. Park, *Adv. Funct. Mater.* **2021**, 31, 2100396; d) S. Li, F. Yang, M. Chen, J. Yang, L. Jiang, Y. Sun, A. N. Graced, S. M. Jain, H. Liu, *Sol. Energy* **2022**, 243, 134.
- [11] a) J.-W. Lee, H.-S. Kim, N.-G. Park, *Acc. Chem. Res.* **2016**, 49, 311; b) W. Zhang, M. Saliba, D. T. Moore, S. K. Pathak, M. T. Hörantner, T. Stergiopoulos, S. D. Stranks, G. E. Eperon, J. A. Alexander-Webber, A. Abate, *Nat. Commun.* **2015**, 6, 6142; c) Q. Chen, H. Zhou, T.-B. Song, S. Luo, Z. Hong, H.-S. Duan, L. Dou, Y. Liu, Y. Yang, *Nano Lett.* **2014**, 14, 4158.
- [12] a) G. Yang, P. Qin, G. Fang, G. Li, *Sol. RRL* **2018**, 2, 1800055; b) B. Lee, C. C. Stoumpos, N. Zhou, F. Hao, C. Malliakas, C.-Y. Yeh, T. J. Marks, M. G. Kanatzidis, R. P. Chang, *J. Am. Chem. Soc.* **2014**, 136, 15379.
- [13] a) G. Kim, H. Min, K. S. Lee, D. Y. Lee, S. M. Yoon, S. I. Seok, *Science* **2020**, 370, 108; b) M. Jeong, I. W. Choi, E. M. Go, Y. Cho, M. Kim, B. Lee, S. Jeong, Y. Jo, H. W. Choi, J. Lee, *Science* **2020**, 369, 1615; c) E. H. Jung, N. J. Jeon, E. Y. Park, C. S. Moon, T. J. Shin, T.-Y. Yang, J. H. Noh, J. Seo, *Nature* **2019**, 567, 511.
- [14] a) F. Zhang, D. H. Kim, K. Zhu, *Curr. Opin. Electrochem.* **2018**, 11, 105; b) A. Thote, I. Jeon, J.-W. Lee, S. Seo, H.-S. Lin, Y. Yang, H. Daiguji, S. Maruyama, Y. Matsuo, *ACS Appl. Energy Mater.* **2019**, 2, 2486.
- [15] a) D. T. Moore, K. W. Tan, H. Sai, K. P. Barteau, U. Wiesner, L. A. Estroff, *Chem. Mater.* **2015**, 27, 3197; b) M. Shahiduzzaman, K. Yamamoto, Y. Furumoto, T. Kuwabara, K. Takahashi, T. Taima, *RSC Adv.* **2015**, 5, 77495.
- [16] a) J. Jang, Y. H. Kim, S. Park, D. Yoo, H. Cho, J. Jang, H. B. Jeong, H. Lee, J. M. Yuk, C. B. Park, *Adv. Mater.* **2021**, 33, 2005255; b) Z. Liu, F. Cao, M. Wang, M. Wang, L. Li, *Angew. Chem. Int. Ed.* **2020**, 59, 4161.
- [17] X. Li, M. Ibrahim Dar, C. Yi, J. Luo, M. Tschumi, S. M. Zakeeruddin, M. K. Nazeeruddin, H. Han, M. Grätzel, *Nat. Chem.* **2015**, 7, 703.
- [18] T. Xue, D. Chen, M. Su, X. Hu, Z. Huang, T. Wu, G. Yu, K.-J. Jiang, Y. Zhang, Y. Song, *J. Mater. Chem. A* **2022**, 10, 18762.
- [19] N. Jiang, B. Xing, Y. Wang, H. Zhang, D. Yin, Y. Liu, Y. Bi, L. Zhang, J. Feng, H. Sun, *Sci. Bull.* **2022**, 67, 794.
- [20] a) N.-R. Jiang, Y.-F. Wang, Q.-F. Dong, C.-D. Ge, Z.-Q. Yang, D. Yin, Y.-F. Liu, Y.-G. Bi, J. Feng, H.-B. Sun, *Sol. RRL* **2021**, 5, 2000821; b) S. Wang, Z. Zhang, Z. Tang, C. Su, W. Huang, Y. Li, G. Xing, *Nano Energy* **2021**, 82, 105712; c) H. Chen, T. Liu, P. Zhou, S. Li, J. Ren, H. He, J. Wang, N. Wang, S. Guo, *Adv. Mater.* **2020**, 32, 1905661; d) Y. Zhao, P. Zhu, M. Wang, S. Huang, Z. Zhao, S. Tan, T. H. Han, J. W. Lee, T. Huang, R. Wang, J. Xue, D. Meng, Y. Huang, J. Marian, J. Zhu, Y. Yang, *Adv. Mater.* **2020**, 32, e1907769.
- [21] a) X. Zeng, T. Zhou, C. Leng, Z. Zang, M. Wang, W. Hu, X. Tang, S. Lu, L. Fang, M. Zhou, *J. Mater. Chem. A* **2017**, 5, 17499; b) D. H. Shin, J. M. Kim, S. H. Shin, S.-H. Choi, *Dyes Pigm.* **2019**, 170, 107630.
- [22] a) K. Chen, Q. Hu, T. Liu, L. Zhao, D. Luo, J. Wu, Y. Zhang, W. Zhang, F. Liu, T. P. Russell, R. Zhu, Q. Gong, *Adv. Mater.* **2016**, 28, 10718; b) S. Dong, Y. Wan, Y. Wang, Y. Yang, Y. Wang, X. Zhang, H. Cao, W. Qin, L. Yang, C. Yao, Z. Ge, S. Yin, *RSC Adv.* **2016**, 6, 57793; c) Y. Chen, T. Chen, L. Dai, *Adv. Mater.* **2015**, 27, 1053.
- [23] Y. He, Y. Yao, S. Li, Q. Sun, Y. Wu, Y. Liu, Z. Li, Y. Cui, C. Ma, Y. Hao, Y. Wu, *IEEE J. Photovoltaics* **2020**, 10, 811.
- [24] a) K. Lee, J. Ryu, H. Yu, J. Yun, J. Lee, J. Jang, *Nanoscale* **2017**, 9, 16249; b) F. Xia, Q. Wu, P. Zhou, Y. Li, X. Chen, Q. Liu, J. Zhu, S. Dai, Y. Lu, S. Yang, *ACS Appl. Mater. Interfaces* **2015**, 7, 13659.
- [25] a) G. Kakavelakis, T. Maksudov, D. Konios, I. Paradisanos, G. Kioseoglou, E. Stratakis, E. Kymakis, *Adv. Energy Mater.* **2017**, 7, 1602120; b) C. Kuang, G. Tang, T. Jiu, H. Yang, H. Liu, B. Li, W. Luo, X. Li, W. Zhang, F. Lu, J. Fang, Y. Li, *Nano Lett.* **2015**, 15, 2756.
- [26] a) Z. Li, N. Liu, Z. Liu, X. Wang, Y. Hu, Q. Xu, S. Li, Z. Qiao, L. Cheng, C. Wang, *Energy Technol.* **2020**, 8, 2000224; b) R. Xu, Z. Wang, W. Xu, X. Xu, J. Wang, Z. Hu, Y. Li, G. Wang, W. Cai, S. Zheng, *Sol. RRL* **2021**, 5, 2100236; c) G. Xu, S. Wang, P. Bi, H. Chen, M. Zhang, R. Xue, X. Hao, Z. Wang, Y. Li, Y. Li, *Sol. RRL* **2020**, 4, 1900249.
- [27] Z. Yang, J. Xie, V. Arivazhagan, K. Xiao, Y. Qiang, K. Huang, M. Hu, C. Cui, X. Yu, D. Yang, *Nano Energy* **2017**, 40, 345.
- [28] a) F. Zhang, C. Xiao, X. Chen, B. W. Larson, S. P. Harvey, J. J. Berry, K. Zhu, *Joule* **2019**, 3, 1452; b) Z. Liu, K. Deng, J. Hu, L. Li, *Angew. Chem.* **2019**, 131, 11621; c) L. Zheng, Y.-H. Chung, Y. Ma, L. Zhang, L. Xiao, Z. Chen, S. Wang, B. Qu, Q. Gong, *Chem. Commun.* **2014**, 50, 11196; d) I. Hwang, I. Jeong, J. Lee, M. J. Ko, K. Yong, *ACS Appl. Mater. Interfaces* **2015**, 7, 17330; e) H. Wang, C. Zhu, L. Liu, S. Ma, P. Liu, J. Wu, C. Shi, Q. Du, Y. Hao, S. Xiang, *Adv. Mater.* **2019**, 31, 1904408.
- [29] R. Xu, Z. Wang, W. Xu, X. Xu, J. Wang, Z. Hu, Y. Li, G. Wang, W. Cai, S. Zheng, G. Wei, F. Huang, S. Yang, *Sol. RRL* **2021**, 5, 2100236.
- [30] J. Kang, R. Huang, S. Guo, G. Han, X. Sun, I. Ismail, C. Ding, F. Li, Q. Luo, Y. Li, C.-Q. Ma, *Sol. Energy* **2021**, 217, 105.
- [31] S. Liu, R. Chen, X. Tian, Z. Yang, J. Zhou, F. Ren, S. Zhang, Y. Zhang, M. Guo, Y. Shen, Z. Liu, W. Chen, *Nano Energy* **2022**, 94, 106935.
- [32] Q. Jiang, Y. Zhao, X. Zhang, X. Yang, Y. Chen, Z. Chu, Q. Ye, X. Li, Z. Yin, J. You, *Nat. Photonics* **2019**, 13, 460.

- [33] P. Caprioglio, M. Stolterfoht, C. M. Wolff, T. Unold, B. Rech, S. Albrecht, D. Neher, *Adv. Energy Mater.* **2019**, *9*, 1901631.
- [34] a) S. Liu, X. Guan, W. Xiao, R. Chen, J. Zhou, F. Ren, J. Wang, W. Chen, S. Li, L. Qiu, Y. Zhao, Z. Liu, W. Chen, *Adv. Funct. Mater.* **2022**, *32*, 2205009; b) R. D. J. Oliver, Y.-H. Lin, A. J. Horn, C. Q. Xia, J. H. Warby, M. B. Johnston, A. J. Ramadan, H. J. Snaith, *ACS Energy Lett.* **2020**, *5*, 3336.
- [35] a) S. Gharibzadeh, P. Fassel, I. M. Hossain, P. Rohrbeck, M. Frericks, M. Schmidt, T. Duong, M. R. Khan, T. Abzieher, B. A. Nejad, F. Schackmar, O. Almora, T. Feeney, R. Singh, D. Fuchs, U. Lemmer, J. P. Hofmann, S. A. L. Weber, U. W. Paetzold, *Energy Environ. Sci.* **2021**, *14*, 5875; b) A. Al-Ashouri, A. Magomedov, M. Roß, M. Jošt, M. Talaikis, G. Chistiakova, T. Bertram, J. A. Márquez, E. Köhnen, E. Kasparavičius, S. Levenco, L. Gil-Escrig, C. J. Hages, R. Schlatmann, B. Rech, T. Malinauskas, T. Unold, C. A. Kaufmann, L. Korte, G. Niaura, V. Getautis, S. Albrecht, *Energy Environ. Sci.* **2019**, *12*, 3356.
- [36] a) X. Zheng, Y. Hou, C. Bao, J. Yin, F. Yuan, Z. Huang, K. Song, J. Liu, J. Troughton, N. Gasparini, C. Zhou, Y. Lin, D.-J. Xue, B. Chen, A. K. Johnston, N. Wei, M. N. Hedhili, M. Wei, A. Y. Alsalloum, P. Maity, B. Turedi, C. Yang, D. Baran, T. D. Anthopoulos, Y. Han, Z.-H. Lu, O. F. Mohammed, F. Gao, E. H. Sargent, O. M. Bakr, *Nat. Energy* **2020**, *5*, 131; b) W.-Q. Wu, P. N. Rudd, Q. Wang, Z. Yang, J. Huang, *Adv. Mater.* **2020**, *32*, 2000995.
- [37] a) W. Kim, J. B. Park, H. Kim, K. Kim, J. Park, S. Cho, H. Lee, Y. Pak, G. Y. Jung, *J. Mater. Chem. A* **2019**, *7*, 20832; b) J. Kang, R. Huang, S. Guo, G. Han, X. Sun, I. Ismail, C. Ding, F. Li, Q. Luo, Y. Li, *Sol. Energy* **2021**, *217*, 105.
- [38] S. Yang, W. Liu, L. Zuo, X. Zhang, T. Ye, J. Chen, C.-Z. Li, G. Wu, H. Chen, *J. Mater. Chem. A* **2016**, *4*, 9430.
- [39] Y. Bai, H. Yu, Z. Zhu, K. Jiang, T. Zhang, N. Zhao, S. Yang, H. Yan, *J. Mater. Chem. A* **2015**, *3*, 9098.
- [40] Y. Huang, S. Wu, R. Chen, S. Fang, S. Zhang, G. Wang, W. Chen, *ACS Appl. Mater. Interfaces* **2019**, *11*, 18415.
- [41] a) T. H. Chowdhury, R. Kaneko, T. Kaneko, K. Sodeyama, J.-J. Lee, A. Islam, *Chem. Eng. J.* **2022**, *431*, 133745; b) H. Xiong, G. DeLuca, Y. Rui, B. Zhang, Y. Li, Q. Zhang, H. Wang, E. Reichmanis, *ACS Appl. Mater. Interfaces* **2018**, *10*, 35385.
- [42] W.-D. Xu, Q. Hu, S. Bai, C. Bao, Y. Miao, Z. Yuan, T. Borzda, A. Barker, E. Tyukalova, Z. Hu, M. Kaweckki, H. Wang, Z. Yan, X. Liu, X. Shi, K. Uvdal, M. Fahlman, W. Zhang, M. Duchamp, F. Gao, *Nat. Photonics* **2019**, *13*, 418.
- [43] S. Liu, X. Guan, W. Xiao, R. Chen, J. Zhou, F. Ren, J. Wang, W. Chen, S. Li, L. Qiu, Y. Zhao, Z. Liu, W. Chen, *Adv. Funct. Mater.* **2022**, *32*, 2205009.
- [44] S. S. Kim, S. Bae, W. H. Jo, *Chem. Commun.* **2015**, *51*, 17413.
- [45] A. Axt, I. M. Hermes, V. W. Bergmann, N. Tausendpfund, S. A. L. Weber, *Beilstein J. Nanotechnol.* **2018**, *9*, 1809.
- [46] a) N. Nicoara, R. Manaligod, P. Jackson, D. Hariskos, W. Witte, G. Sozzi, R. Menozzi, S. Sadewasser, *Nat. Commun.* **2019**, *10*, 3980; b) T.-X. Qin, E.-M. You, M.-X. Zhang, P. Zheng, X.-F. Huang, S.-Y. Ding, B.-W. Mao, Z.-Q. Tian, *Light Sci. Appl.* **2021**, *10*, 84.
- [47] S. Zhang, W. Chen, S. Wu, R. Chen, Z. Liu, Y. Huang, Z. Yang, H. Zhu, J. Li, L. Han, W. Chen, *ACS Appl. Mater. Interfaces* **2019**, *11*, 43303.
- [48] S. Yang, S. Chen, E. Mosconi, Y. Fang, X. Xiao, C. Wang, Y. Zhou, Z. Yu, J. Zhao, Y. Gao, F. De Angelis, J. Huang, *Science* **2019**, *365*, 473.
- [49] J.-E. Kim, S.-S. Kim, C. Zuo, M. Gao, D. Vak, D.-Y. Kim, *Adv. Funct. Mater.* **2019**, *29*, 1809194.
- [50] Y. Wu, G. Xu, J. Xi, Y. Shen, X. Wu, X. Tang, J. Ding, H. Yang, Q. Cheng, Z. Chen, Y. Li, Y. Li, *Joule* **2023**, *7*, 398.
- [51] W. Chen, Y. Wu, Y. Yue, J. Liu, W. Zhang, X. Yang, H. Chen, E. Bi, I. Ashraful, M. Grätzel, L. Han, *Science* **2015**, *350*, 944.